CHEMIJA
2025. Vol. 36. No. 2. P. 88–98

ISSN 0235-7216 eISSN 2424-4538
DOI: https://doi.org/10.6001/chemija.2025.36.2.5

On the optimisation of the broadband NIR emitter $LiScO_2:Cr^{3+}$

Leoni Frehmeyer,

Tim Pier*,

Thomas Jüstel*

FH Münster University of Applied Sciences,
Stegerwaldstr. 39,
D-48565 Steinfurt, Germany

Cr^{3+}-activated $LiScO_2$ has emerged as a promising near-infrared (NIR) phosphor with potential applications in medical and optical technologies. In this study, the luminescence properties of $LiScO_2:Cr^{3+}$ were optimised through systematic cation substitutions. The effect of Cr^{3+}-concentration (0.5 to 5 mol.%) was investigated, along with substitutions of Sc^{3+} by Al^{3+} and Li^{+} by Na^{+}. The synthesised phosphors were characterised upon using X-ray diffraction (XRD), reflectance spectroscopy, fluorescence spectroscopy, and decay curve analysis. The results demonstrate that optimal Cr^{3+} doping concentrations enhance NIR emission, whereas excessive doping leads to concentration quenching. Substitutions of Sc^{3+} with Al^{3+} and Li^{+} with Na^{+} impact crystal field strength and luminescence properties. These findings contribute to the development of efficient broadband NIR phosphors for future applications.

Keywords: NIR phosphors, photoluminescence, scandate, trivalent chromium, time-dependent spectroscopy

INTRODUCTION

The development of innovative materials for medical applications has gained considerable importance in recent decades, particularly in the field of near-infrared radiation (NIR) for therapeutic purposes. A promising area of application for NIR phosphors is the treatment of Sjögren's syndrome, a chronic autoimmune disease characterised primarily by inflammation and dysfunction of the lacrimal and salivary glands. This disorder leads to pronounced symptoms such as dry eyes or dry mouth and significantly impairs the quality of life of those affected [1, 2].

Current research shows that exposure to specific wavelengths of NIR radiation can relieve inflammation and promote blood flow in damaged glandular tissues, improving the symptoms of the disorder. Regarding this background, the synthesis and optimisation of NIR phosphors, especially comprising broadband emitters such as Cr^{3+}, offer a promising approach to tackle this issue [2, 3].

The aim of this work was to investigate cation exchange based host lattice modifications of the phosphor $LiScO_2:Cr^{3+}$ and to further analyse how the exchange of ions affects the optical properties of the phosphor. In order to determine how the Cr^{3+} content influences the luminescence properties, a Cr^{3+} concentration series in the range from 0.5 to 5 mol.% was also used.

EXPERIMENTAL

Sample preparation

For the synthesis of $LiScO_2:Cr^{3+}$ with the respective substitution of Li^{+} and Sc^{3+} ions by Na^{+} and Al^{3+} ions, i.e. $(Li_{1-x}Na_x)ScO_2:Cr^{3+}$ and $Li(Sc_{1-x}Al_x)O_2:Cr^{3+}$ (x = 0.01, 0.02, 0.05, 0.07, 0.10), a solid-state reaction was used. The samples were synthesised using Li_2CO_3 (Alfa Aesar, 99%), Sc_2O_3

---

* Corresponding author. Email: timpier@fh-muenster.de

(Treibacher, 99.99%), Cr_2O_3 (Alfa Aesar, 99.95%), Na_2CO_3 (Merck KGaA, 99.9%) and Al_2O_3 (Alfa Aesar, 99.95%) as educts. Additionally, a Cr^{3+} concentration series (x = 0.005, 0.010, 0.015, 0.020, 0.025, 0.030, 0.035, 0.040, 0.045, 0.050) was prepared. For this purpose, all starting materials were weighed stoichiometrically and mixed with ethanol, supplemented by a 5 mol.% excess of lithium carbonate to account for evaporation during the annealing process. The mixture was homogenised for 1 h using a ball mill. Once the ethanol had completely evaporated, the precursor was transferred into a corundum sarcophagus crucible and annealed at 1200°C for 8 h in a tube furnace with a heating rate of 5 K/min. To prevent oxidation of chromium, the reaction was carried out under a forming gas atmosphere (95% N_2/5% H_2).

Analytical measurements

Powder X-ray diffraction was employed to judge the crystal structure and phase purity of the samples [4, 5]. The diffractometer used was the MiniFlex II from Rigaku. X-rays were generated using a copper X-ray tube, which was operated at a voltage of 30 kV and a current of 15 mA, and operated in Bragg–Brentano geometry. Measurements were conducted at a scan speed of 2.5°/min with a step width of 0.02° over a 2θ range from 10 to 80°. To identify the resulting phases, the measured diffractograms were compared with reference diffractograms from the Pearson's Crystal Data database.

Reflection measurements were performed on an Edinburgh Instruments FS920 spectrometer, combined with a Teflon-coated integrating sphere. For the measurement, a 450 W Xe900 arc lamp from Edinburgh Instruments and a Peltier-cooled R928 detector from Hamamatsu, operated at –20°C, were used. The samples were measured in a range from 250 to 800 nm with a step width of 1.0 nm. $BaSO_4$ (99.99%, Sigma-Aldrich) was used as the white reflectance standard.

Excitation and emission spectra were recorded using an Edinburgh Instruments FLS920. A 450 W xenon discharge lamp served as the excitation source, while a Peltier-cooled SP-PMT R2658P detector from Hamamatsu, operated at –20°C, was used for radiation detection. The emission spectra were corrected using a correction file from the National Physical Laboratory (NPL). Excitation spectra were corrected via a reference detector that operated in parallel during all excitation measurements. Temperature-dependent emission spectra in a range from 77 to 500 K were recorded using a liquid nitrogen cooled Microstat N2 cryostat produced by Oxford Instruments. For measurements below 100 K, a helium-cooled cryostat (Oxford Instruments Optistat AC-V 12) was used. Time-resolved spectroscopy was used to analyse the decay behaviour. The measurements were conducted using the same FLS920 spectrometer, equipped with a pulsed 445 nm laser diode (Edinburgh Instruments) as the excitation source.

The magnetic susceptibility was measured using a Faraday balance from Alfa Aesar. The measurement result, which refers to the 1 cm^3 sample volume, is given in 'electromagnetic units' (emu).

RESULTS AND DISCUSSION

$LiScO_2$ crystallises in the tetragonal space group $I4_1/amd$ – D_4h^{19} (Schoenflies notation). In this space group, the atomic positions are occupied as follows: 4 Sc at 4(a), 4 Li at 4(b) and 8 O at 8(e) [6]. This means that in the host lattice $LiScO_2$, the Sc^{3+} and Li^+ ions are sixfold coordinated, each surrounded by six oxygen atoms, forming distorted octahedra. As a result, the Cr^{3+} ions experience a distorted octahedral crystal field [1, 3]. When doped, the Cr^{3+} ions occupy the position of Sc^{3+}, and this can be explained by Goldschmidt's rules regarding valency and ionic radii.

X-ray diffraction (XRD) measurements

The X-ray diffraction patterns of the Cr^{3+} concentration series are presented in Fig. 1. Comparison with the $LiScO_2$ reference indicates that all samples have formed the desired tetragonal phase. However, the diffraction patterns of the samples with Cr^{3+} concentrations of 4.5 and 5.0 mol.% exhibit weak reflexes at 2θ = 18.5°, which can be assigned to the $LiCrO_2$ impurity phase based on comparison with an additional reference X-ray diffraction pattern. As the intensity of the reflections at 2θ = 18.5° increases with increasing Cr^{3+} concentration, it suggests that the amount of impurity phase also increases with rising Cr^{3+} concentration.

The X-ray diffraction patterns of the substitution series $(Li_{1-x}Na_x)Sc_{0.99}O_2$:$Cr_{0.01}$ are presented in

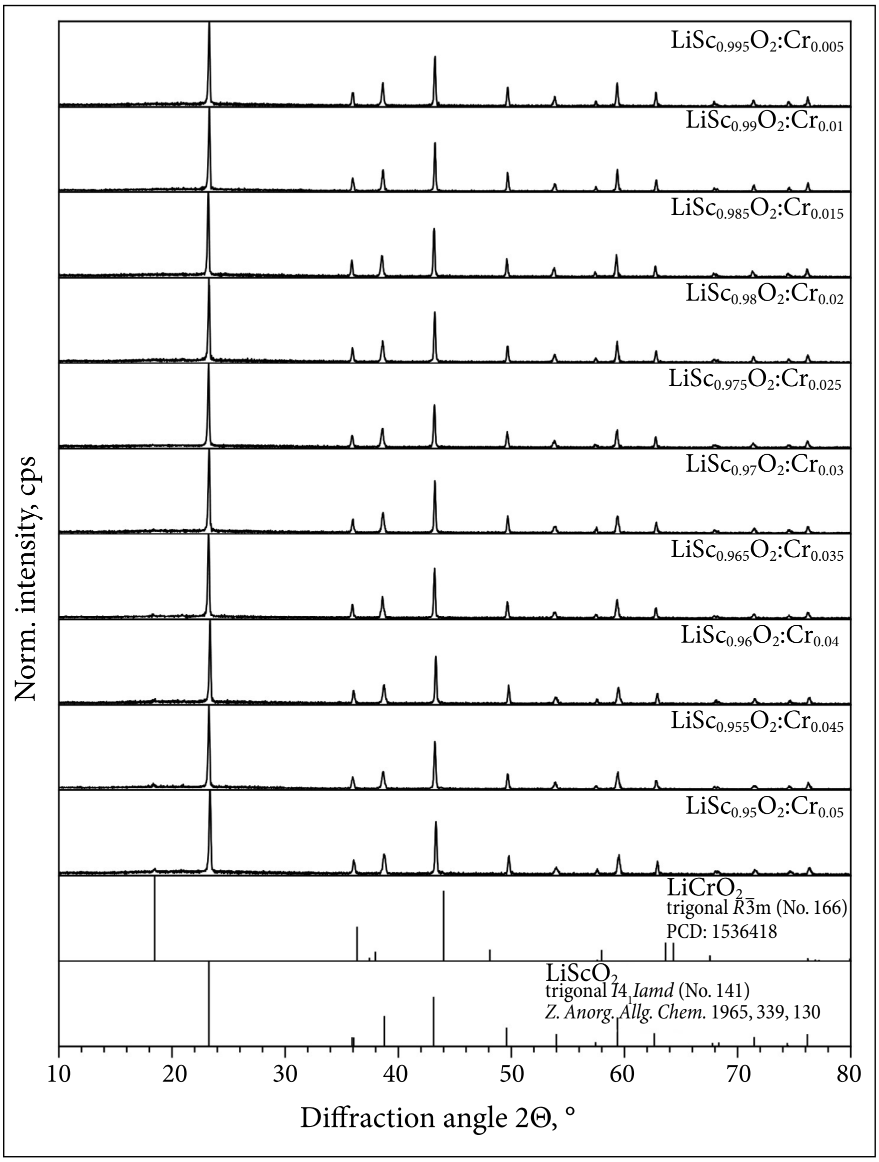

Fig. 1. Powder X-ray diffraction (XRD) measurements of $LiSc_{1-x}O_2:Cr_x$ with x values of 0.005–0.050

Fig. 2a. The comparison with the $LiScO_2$ reference indicates that the desired phase has been formed. However, the samples with Na^+ concentrations of 7 and 10 mol.% display reflexes at 2θ = 32.0°, and the sample with a Na^+ concentration of 10 mol.% exhibit an additional reflex at 2θ = 21.5°. The comparison with another reference suggests that a Sc_2O_3 impurity phase has formed, and its intensity increases with increasing Na^+ concentration. The X-ray diffraction patterns of the substitution series $Li(Sc_{1-x}Al_x)O_2:Cr_{0.01}$ are presented in Fig. 2b. Comparison with the $LiScO_2$ reference indicates that the desired phase has been formed. As observed in the Na^+ substitution series, additional reflections appear at Al^{3+} concentrations above 7 mol.%, specifically at 2θ = 22.6°, 33.7° and 35.0°.

Diffuse reflectance spectroscopy

Figure 3 shows the reflectance spectra of the Cr^{3+} concentration series. No absorption bands are observed in the visible wavelength range of the pristine host lattice $LiScO_2$. At a Cr^{3+} concentration of 0.05 mol.%, two absorption bands of Cr^{3+} become visible, corresponding to the transitions $^4A_2g(^4F) \rightarrow {}^4T_1g(^4F)$ (375–555 nm) and $^4A_2g(^4F) \rightarrow {}^4T_2g(^4F)$ (555–800 nm). Furthermore, a characteristic chromium line is observed at 713 nm, which corresponds to the spin-forbidden $^4A_2 \rightarrow {}^2Eg$ transition.

The absorption intensity increases with increasing Cr^{3+} concentration, which can be attributed to the growing number of luminescence centres. This effect is also reflected in a change of the body

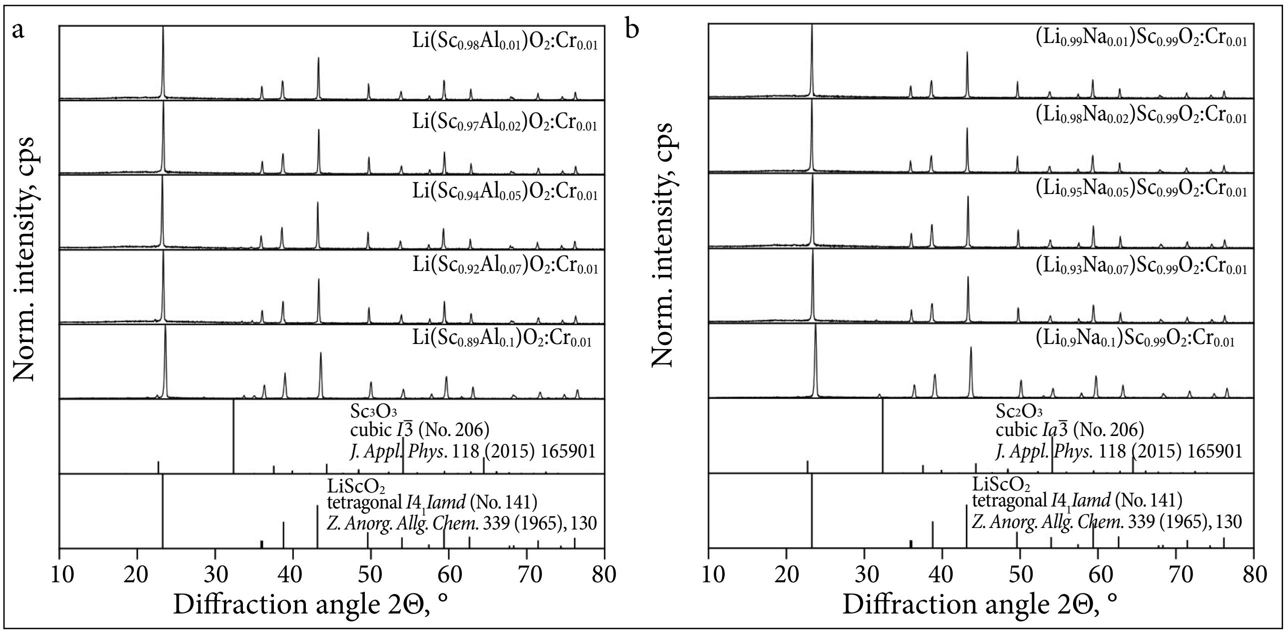

Fig. 2. Powder X-ray diffraction (XRD) measurements of (a) $(Li_{1-x}Na_x)Sc_{0.99}O_2:Cr_{0.01}$ and (b) $Li(Sc_{1-x}Al_x)O_2:Cr_{0.01}$ with *x* values of 0.01–0.10

colour of the polycrystalline samples, i.e. the rose colour of the powders intensifies with increasing Cr^{3+} concentration. Since the position of the absorption maxima does not change with increasing Cr^{3+} concentration, the influence on the crystal field environment is negligible [3].

As seen in the reflectance spectra of the Cr^{3+} concentration series (Fig. 3), the reflectance spectra of the Na^+ concentration series (Fig. 4) also exhibit the two absorption bands of Cr^{3+} and the chromium line at 713 nm. The most intense absorption bands are observed for the sample without Na^+. The samples with a Na^+ concentration of 5 mol.% or higher show an additional absorption band in the wavelength range of 350 to 430 nm, albeit with a low intensity.

The reflectance spectra of the Al^{3+} substitution series (Fig. 5) also display the two characteristic absorption bands of Cr^{3+} and the chromium line at 713 nm. Notably, the reflectance spectra of the Al^{3+} substitution series differ from those of the Na^+ substitution series in that the unsubstituted sample exhibits the lowest intensities of the two absorption bands. A closer examination of the individual spectra reveals that the absorption intensity increases with increasing Al^{3+} concentration.

Fluorescence spectroscopy

In Fig. 6b, the emission spectra of the Cr^{3+} concentration series are shown. With increasing Cr^{3+} concentration, a redshift of the emission peak is

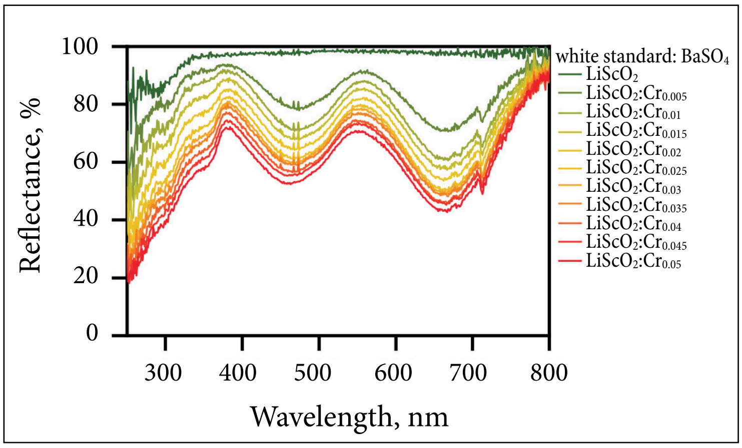

Fig. 3. Reflection spectra of $LiSc_{1-x}O_2:Cr_x$ with *x* values of 0.00–0.050

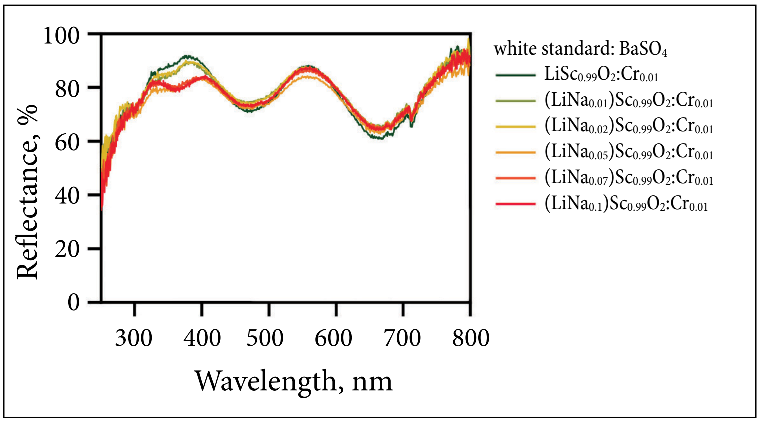

Fig. 4. Reflection spectra of $(Li_{1-x}Na_x)Sc_{0.99}O_2:Cr_{0.01}$ with x values of 0.00–0.10

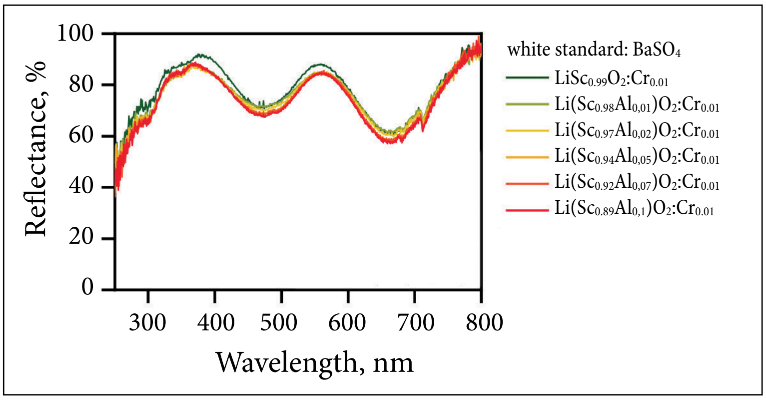

Fig. 5. Reflection spectra of $Li(Sc_{1-x}Al_x)O_2:Cr_{0.01}$ with $x = 0.01–0.1$

observed, spanning a wavelength range of 810 to 833 nm. Since the Cr^{3+} ion occupies the lattice site of the Sc^{3+} ion, an increase in crystal field strength occurs due to the contraction of the lattice caused by the smaller ionic radius of the Cr^{3+} ion compared to the Sc^{3+} ion [7, 8]. A redshift resulting from a weakening of the crystal field can thus be excluded. The most likely explanation for the redshift is the increasing formation of Cr^{3+}–Cr^{3+} ion pairs with increasing Cr^{3+} concentration [3]. The emission intensity of the emission integral and the peak intensity are plotted against the Cr^{3+} concentration. Initially, the emission intensity increases with increasing Cr^{3+} concentration until it reaches its maximum at a concentration of 1.5 mol.%. Subsequently, a decrease in intensity occurs due to concentration quenching (Fig. 7a) [3, 9–11].

The excitation spectra of the Cr^{3+} concentration series are presented in Fig. 6b. The two excitation bands with peak intensities at 480 and 615 nm correspond to the parity-forbidden transitions $^4A_{2g}(^4F) \rightarrow {}^4T_{1g}(^4F)$ and $^4A_{2g}(^4F) \rightarrow {}^4T_{2g}(^4F)$, respectively. The excitation band for the $^4A_{2g}(^4F) \rightarrow {}^4T_{1g}(^4P)$ transition is visible in the 290 to 320 nm wavelength range. A peak at 710 nm is attributed to the spin-forbidden $^4A_2 \rightarrow {}^2Eg$ transition. Initially, the intensity increases with rising Cr^{3+} concentration but decreases beyond 1.5 mol.%, which is consistent with concentration quenching [3, 9–11]. Moreover, it is worth noting that the two samples with Cr^{3+} concentrations of 4.5 and 5.0 mol.% are not phase-pure.

The emission spectra of the substitution series of Li^+ with Na^+ are shown in Fig. 6d. A significant decrease in emission intensity is observed as soon as Li^+ ions are replaced with Na^+ ions. The compound with a Na^+ concentration of 5 mol.% exhibits the lowest emission intensity. With increasing Na^+ concentrations, the emission intensity increases (Fig. 7b); however, it should be noted that the samples are no longer phase-pure beyond a Na^+ concentration of 7 mol.%. The incorporation of Na^+ ions, which have a larger ionic radius than Li^+ ions into the $LiScO_2$ lattice leads to an increase in

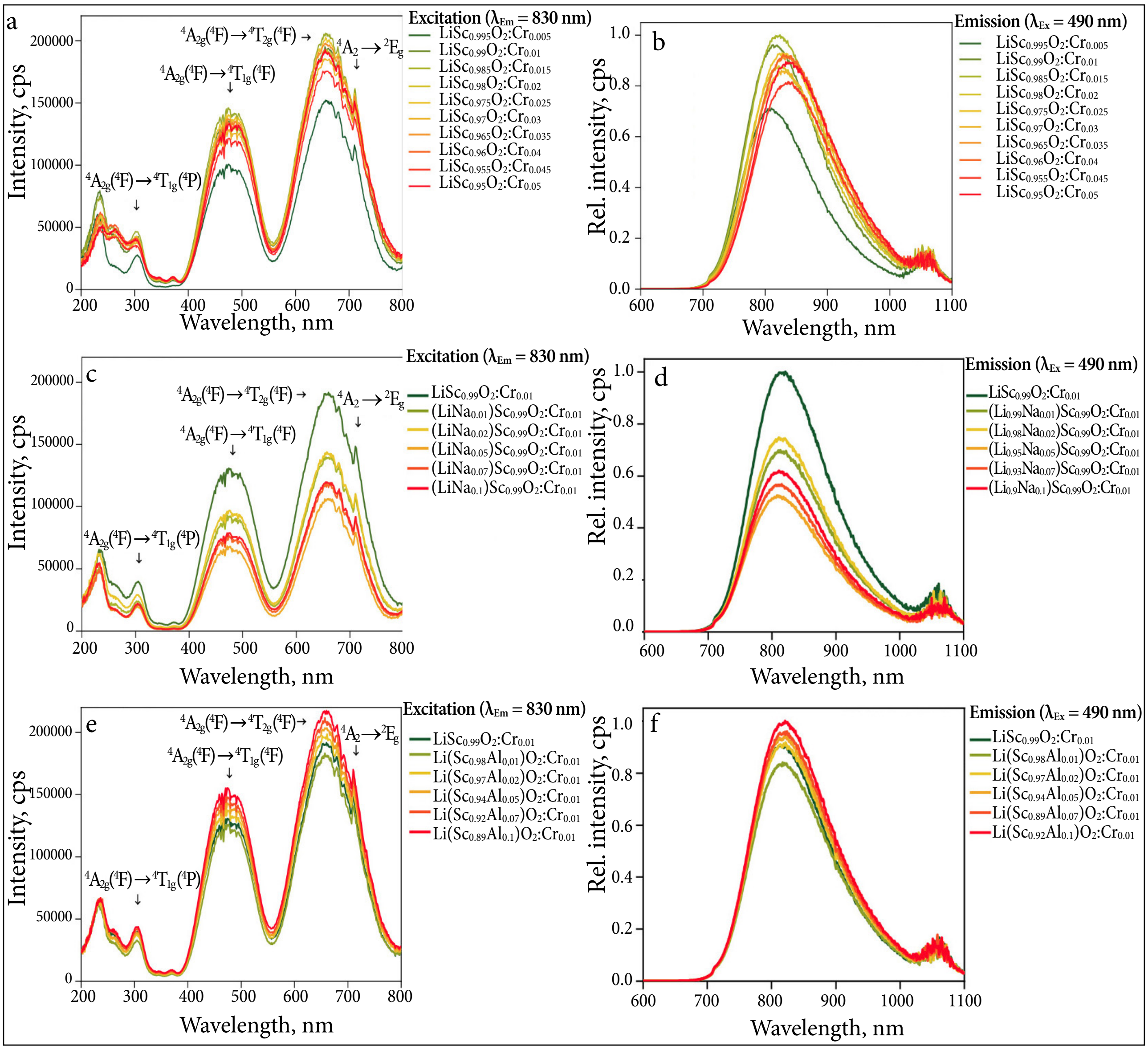

Fig. 6. Emission spectra of (a) $LiSc_{1-x}O_2:Cr_x$ with *x* values of 0.005–0.05, (c) $(Li_{1-x}Na_x)Sc_{0.99}:Cr_{0.01}$ and (e) $Li(Sc_{1-x}Al_x)O_2:Cr_{0.01}$ with *x* values of 0.00–0.10, and excitation spectra of (b) $LiSc_{1-x}O_2:Cr_x$ with *x* values of 0.005–0.05, (d) $(Li_{1-x}Na_x)Sc_{0.99}:Cr_{0.01}$ and (f) $Li(Sc_{1-x}Al_x)O_2:Cr_{0.01}$ with *x* values of 0.00–0.10

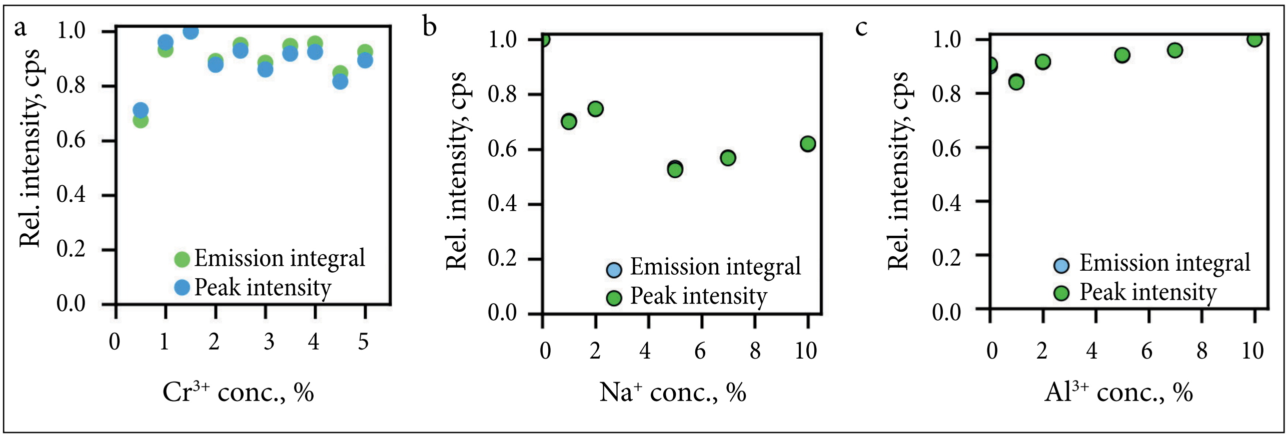

Fig. 7. Emission integral and peak intensity of (a) $LiSc_{1-x}O_2:Cr_x$ with *x* values of 0.005–0.05, (b) $(Li_{1-x}Na_x)Sc_{0.99}:Cr_{0.01}$ and (c) $Li(Sc_{1-x}Al_x)O_2:Cr_{0.01}$ with x values of 0.00–0.10

the Cr–O atomic distance within the crystal lattice, thereby reducing the crystal field strength around the Cr^{3+} ion [7, 8, 12]. The reduction in crystal field strength results in a blue shift of the maximum emission wavelength [13]. The excitation spectra of the Na^+ substitution series are presented in Fig. 6c. Similar to those in Fig. 6a, the two excitation bands corresponding to the parity-forbidden $^4A_{2g}(^4F) \rightarrow {}^4T_{1g}(^4F)$ and $^4A_{2g}(^4F) \rightarrow {}^4T_{2g}(^4F)$ transitions of Cr^{3+} are observed, with peak intensities at 480 and 615 nm, respectively. The peak at 713 nm, likely associated with the spin-forbidden $^4A_2 \rightarrow {}^2E_g$ transition, is also visible in each excitation spectrum [3]. The sample without Na^+ substitution exhibits the highest excitation intensity. In agreement with the emission spectra, the compound with a Na^+ concentration of 5 mol.% displays the lowest intensity, and the intensity increases with rising Na^+ concentrations.

In contrast to the emission spectra of the Li^+ substitution series with Na^+, an approximately linear increase in emission intensity is observed through substitution of Sc^{3+} with Al^{3+} in Fig. 6f. The emission band with the lowest emission intensity still lies at an Al^{3+} concentration of 1 mol.%, which may be an outlier. Since the two highest Al^{3+} concentrations are not phase-pure, they are not considered further despite their higher emission intensity. The incorporation of Al^{3+} ions, which have a smaller ionic radius than Sc^{3+} [7, 8] into the $LiScO_2$ lattice leads to a reduction in the Cr–O atomic distance within the crystal lattice, thereby increasing the crystal field strength around the Cr^{3+} ion [12]. The increase in crystal field strength due to this exchange results in a redshift of the emission peak [13]. The increase in emission intensity upon substitution of Sc^{3+} with Al^{3+} in $LiScO_2$ may be explained by approaching an eutectic composition. An eutectic is a specific composition in a binary system where the two components are in an optimal ratio and exhibit a lower melting point compared to the individual components. A decrease in the melting point could lead to an increase in crystallinity, which may be the cause of the increased emission intensity. The excitation spectra of the Al^{3+} substitution series, presented in Fig. 6e, resemble those previously shown (Fig. 6a, c), displaying the two excitation bands that can be assigned to the parity-forbidden $^4A_{2g}(^4F) \rightarrow {}^4T_{1g}(^4F)$ and $^4A_{2g}(^4F) \rightarrow {}^4T_{2g}(^4F)$ transitions of Cr^{3+}. The maxima of these bands occur at 480 and 617 nm, respectively. Additionally, the peak at 710 nm, likely corresponding to the spin-forbidden $^4A_2 \rightarrow {}^2$Eg transition, is visible in each excitation spectrum [3]. With the exception of the sample with an Al^{3+} concentration of 1 mol.%, the excitation intensity increases with rising Al^{3+} concentration.

Temperature-dependent emission spectroscopy

The emission spectra measured at various temperatures between 77 and 500 K, as presented in Fig. 8, demonstrate the impact of temperature on the emission properties. Clearly, the emission intensity decreases as the temperature increases due to thermal quenching [14, 15]. Furthermore, it is

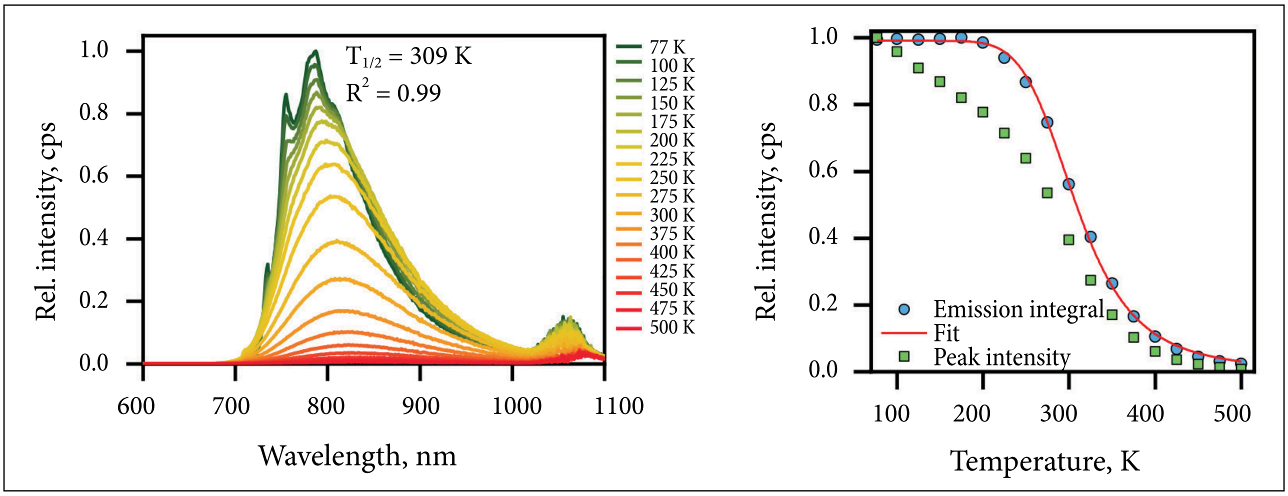

Fig. 8. Temperature-dependent emission spectra of $LiSc_{0.99}O_2:Cr_{0.01}$ at temperatures ranging from 77 to 500 K

evident that at low temperatures, the emission spectrum splits into three distinct bands. As the temperature rises, the emission bands undergo a slight broadening, which leads to overlap and ultimately results in a single band, giving rise to a coalescence phenomenon.

Decay curves

Figure 9a shows the recorded decay curves of two samples with the highest and lowest Cr^{3+} concentrations from the Cr^{3+} concentration series. On Fig. 9b, the diagram plots the decay times of all samples in the Cr^{3+} concentration series against the Cr^{3+} concentration. The two samples with the lowest Cr^{3+} concentrations exhibit a monoexponential decay. Above a Cr^{3+} concentration of 2 mol.%, a bi-exponential decay of the decay times occurs, which could indicate the formation of Cr^{3+}–Cr^{3+} pairs [3]. As the Cr^{3+} concentration increases, the corresponding decay time shortens, primarily due to concentration quenching.

Table 1 lists the decay times along with the percentage contributions of the Cr^{3+} concentration. Notably, as the Cr^{3+} concentration increases, the fraction of τ_1 decreases while the fraction of τ_2 increases. Additionally, it is again evident that both decay times, τ_1 and τ_2, decrease with increasing Cr^{3+} concentration.

Figure 10a displays the decay curves of $(Li_{0.98}Na_{0.02})Sc_{0.99}O_2{:}Cr_{0.01}$ and $LiSc_{0.99}O_2$: $Cr_{0.01}$ o. The plot on Fig. 10b shows the decay time as a function of Na^+ concentration. No significant influence of Na^+ concentration on the decay time is observed. Furthermore, the relative contributions of τ_1 and τ_2, as well as the decay times listed in Table 2, do not exhibit any unusual features.

Figure 10c presents the decay curves of $Li(Sc_{0.97}Al_{0.02})O_2{:}Cr_{0.01}$ and $LiSc_{0.99}O_2{:}Cr_{0.01}$, which,

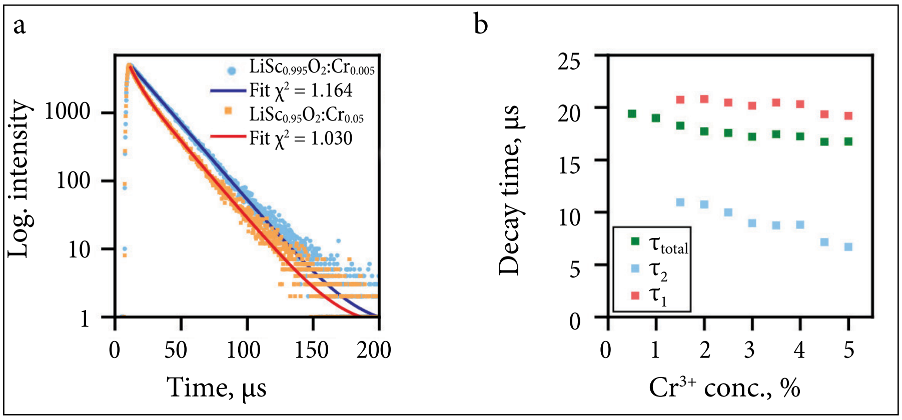

Fig. 9. (a) Decay curves for $LiSc_{0.995}O_2{:}Cr_{0.005}$ and $LiSc_{0.95}O_2{:}Cr_{0.05}$; (b) decay times for $LiSc_{1-x}O_2{:}Cr_x$ with *x* values of 0.005–0.050

Table 1. **Results of the decay curve measurements of $LiSc_{1-x}O_2{:}Cr_x$ with *x* values of 0.005, 0.010, 0.015, 0.020, 0.025, 0.030, 0.035, 0.040, 0.045 and 0.050**

Cr^{3+}-conc., %	Relative amplitude of τ_1, %	Relative amplitude of τ_2, %	τ_1 decay time, µs	τ_2 decay time, µs
0.5	100.00	0.00	19.42	0.00
1.0	100.00	0.00	18.97	0.00
1.5	25.38	74.62	10.93	20.75
2.0	30.76	69.24	10.73	20.79
2.5	27.61	72.39	9.98	20.47
3.0	26.41	73.59	8.95	20.17
3.5	25.69	74.31	8.75	20.46
4.0	26.75	73.25	8.79	20.31
4.5	21.57	78.43	7.14	19.35
5.0	19.49	80.51	6.67	19.19

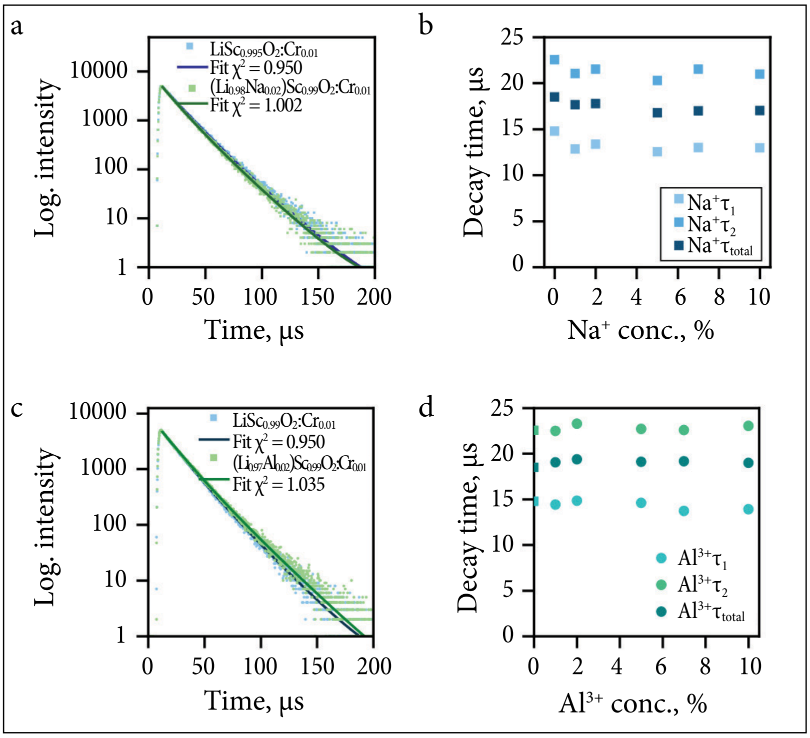

Fig. 10. Decay curves for (a) $LiSc_{0.99}:Cr_{0.01}$ and $(Li_{0.98}Na_{0.02})Sc_{0.99}:Cr_{0.01}$ and (c) $LiSc_{0.99}:Cr_{0.01}$ and $Li(Sc_{0.97}Al_{0.02})O_2:Cr_{0.01}$ and decay times for (b) $(Li_{1-x}Na_x)Sc_{0.99}:Cr_{0.01}$ and (d) $Li(Sc_{1-x}Al_x)O_2:Cr_{0.01}$ with x values of 0.00–0.10.

Table 2. **Results of the decay curve measurements of $(Li_{1-x}Na_x)Sc_{0.99}O_2:Cr_{0.01}$ with x values of 0.00, 0.01, 0.02, 0.05, 0.07 and 0.10**

Na^+-conc., %	Relative amplitude of τ_1, %	Relative amplitude of τ_2, %	τ_1 decay time, μs	τ_2 decay time, μs
0.0	52.41	47.59	14.79	22.56
1.0	41.39	58.61	12.86	21.05
2.0	46.08	53.92	13.37	21.51
5.0	45.31	54.69	12.56	20.29
7.0	53.16	46.84	12.99	21.52
10.0	49.27	50.73	12.96	20.98

like Fig. 10a, show no influence of Al^{3+} concentration on the decay time, as seen on Fig. 10d. Furthermore, the relative contributions of τ_1 and τ_2, tabulated in Table 3, do not display any discernible trend.

Magnetic susceptibility

Figure 11 shows the magnetic susceptibility as a function of Cr^{3+} concentration, where this property is plotted against the Cr^{3+} concentration.

Table 3. **Results of the decay curve measurements of $Li(Sc_{1-x}Al_x)O_2:Cr_{0.01}$ with x values of 0.01–0.10**

Al^{3+}-conc., %	Relative amplitude of τ_1, %	Relative amplitude of τ_2, %	τ_1 decay time, μs	τ_2 decay time, μs
0.0	52.41	47.59	14.79	22.56
1.0	42.60	57.40	14.41	22.50
2.0	46.04	53.96	14.83	23.28
5.0	44.30	55.70	14.60	22.70
7.0	38.64	61.36	13.72	22.59
10.0	44.41	55.59	13.91	23.03

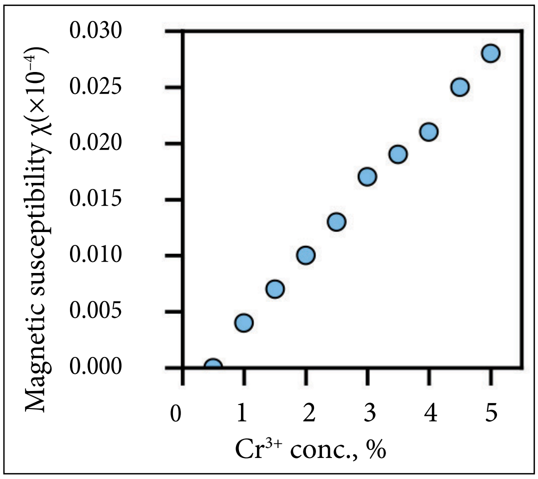

Fig. 11. Magnetic susceptibility of $LiSc_{1-x}O_2:Cr_x$ with x values of 0.000–0.05.

It is evident that the magnetic susceptibility increases linearly with rising Cr^{3+} concentration, indicating that the samples exhibit the classic Curie paramagnetism. This implies that chromium pairing begins to occur at a Cr^{3+} concentration of 1 mol.%.

Racah parameter

The calculation of the Racah parameter B for $LiSc_{0.99}O_2:Cr_{0.01}$ requires the extraction of ν_1 and ν_2 values from the respective excitation spectra, which are then used in the relevant formula [16, 18]. To improve the accuracy of the maxima determination, the excitation spectra were fitted with two Gaussian curves (refer to Fig. 12).

The optical properties of the $LiSc_{0.99}O_2:Cr_{0.01}$ material are characterised by excitation wavelengths of λ_1 = 663 nm and λ_2 = 477 nm, and an emission wavelength of λ = 830 nm. The nephelauxetic effect (Greek for 'cloud broadening') describes the partial shift of electron density from a central atom to the surrounding ligands [19]. The nephelauxetic parameter β can be calculated from the Racah parameter [20]. The calculated Racah parameter B is 583 cm^{-1}, the nephelauxetic parameter β is 0.59, and the crystal field strength Dq/B is 25.87, indicating the local crystal field environment around the Cr^{3+} ion.

CONCLUSIONS

Within the framework of this work, it was possible to synthesise and characterise Cr^{3+}-activated $LiScO_2$. The same was achieved for the substitution of this compound with both Al^{3+} and Na^+. $LiScO_2:Cr^{3+}$ is a broadband near-infrared (NIR) emitter, exhibiting an emission spectrum ranging from approximately 700 to 1050 nm.

To dope $LiScO_2$ with Cr^{3+}, a concentration series was initially prepared to determine the optimal Cr^{3+} concentration. The compound with a Cr^{3+} concentration of 1.5 mol.% showed the highest

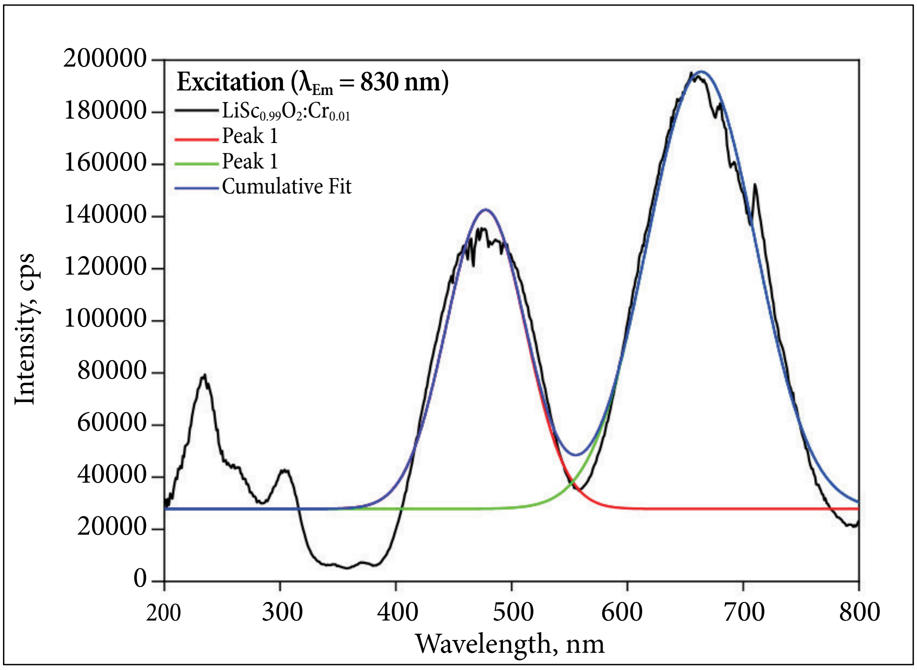

Fig. 12. Fitted excitation spectrum of $LiSc_{0.99}O_2:Cr_{0.01}$ using Gaussian curves

emission intensity. For substitution with Al^{3+} and Na^+, a Cr^{3+} concentration of 1 mol.% was chosen. Therefore, a substitution series was produced and characterised for each. The compounds containing Na^+ exhibited a reduction in emission intensity compared to the starting compound without Na^+ substitution. In contrast, substitution with Al^{3+} resulted in an increase in emission. The Al^{3+} concentration of the compound with the highest emission intensity, which is also phase-pure, is 5.0 mol.%. Although the two subsequent Al^{3+} concentrations in the series could exhibit even higher emission intensities, they were no longer phase-pure. For both the efficiency and economic viability of this phosphor, it makes sense to perform substitution with Al^{3+}.

In further work, the synthesis conditions could be further optimised for higher Al^{3+} concentrations, for example, through the use of a fluxing agent, so that no secondary phases are present. Additionally, the combination of the two ions used for substitution could be investigated. Another possibility would be to consider the substitution of other ions.

Received 10 March 2025
Accepted 24 March 2025

References

1. R. I. Fox, *Lancet*, **366**, 321(2005).
2. L. Chen, Q. Liu, P. Li, et al., *Adv. Therap.*, **7** (2024).
3. Y. Qin, J. Zhong, F. Du, J. Wen, Z. Lin, W. Zhao, *J. Lumin.*, **257**, 119758 (2023).
4. W. Kleber, J. Bohm, D. Klimm, M. Mühlberg, B. Winkler, *Einführung in die Kristallographie*, 20th edn., De Gruyter (2020).
5. L. Spieß, G. Teichert, R. Schwarzer, H. Behnken, C. Genzel, *Moderne Röntgenbeugung*, Springer Fachmedien Wiesbaden, Wiesbaden (2019).
6. R. Hoppe, B. Schepers, H.-J. Rohrborn, E. Vielhaber, *Z. Anorg. Allg. Chem.*, **339**, 130 (1965).
7. J. R. Rumble, D. R. Lide, T. J. Bruno (ed.), *CRC Handbook of Chemistry and Physics*, 100th edn., CRC Press Taylor & Francis Group, Boca Raton, London, New York (2019).
8. A. F. Holleman, N. Wiberg, *Lehrbuch der anorganischen Chemie*, De Gruyter, Berlin (2007).
9. F. Schröder, *Blau-zu-UV-Aufwärtskonversion in Pr(III) Aktivierten Leuchtstoffen*, Westfälischen Wilhelms-Universität Münster (2023).
10. W. M. Yen, S. Shionoya, H. Yamamoto, *Phosphor Handbook*, 2nd edn., CRC Press/Taylor & Francis, Boca Raton, Florida (2007).
11. G. Blasse, B. C. Grabmaier, *Luminescent Materials*, Springer Berlin Heidelberg, Berlin, Heidelberg (1994).
12. N. Majewska, A. Muñoz, R.-S. Liu, S. Mahlik, *Chem. Mater.*, **35**, 4680 (2023).
13. V. Stasiv, Y. Zhydachevskyy, V. Stadnik, et al., *J. Alloys Compd.* (2024).
14. F. Baur, D. Enseling, T. Jüstel, *Optical Spectroscopy: Characterisation of Inorganic LED Phosphors* (2021).
15. S. N. Menon, S. Y. Kadam, D. K. Koul, *J. Lumin.*, **216**, 116716 (2019).
16. P. Dang, Y. Wei, D. Liu, G. Li, J. Lin, *Adv. Opt. Mater.*, **11** (2023).
17. G. Wei, P. Li, R. Li, et al., *Adv. Opt. Mater.*, **11** (2023).
18. S. L. Reddy, T. Endo, G. S. Reddy, in: M. Akhyar Farrukh (ed.), *Advanced Aspects of Spectroscopy*, InTech (2012).
19. S. S. T. Jüstel, *Leuchtstoffe, Lichtquellen, Laser, Lumineszenz*, Springer Berlin Heidelberg, Berlin, Heidelberg (2019).
20. J. E. Huheey, E. A. Keiter, R. L. Keiter, *Anorganische Chemie: Prinzipien von Struktur und Reaktivität*, De Gruyter (2012).

Leoni Frehmeyer, Tim Pier, Thomas Jüstel

PLAČIAJUOSČIO ARTIMOJO INFRARAUDONOJO SPINDULIAVIMO SPINDULIUOTĖS LIScO$_2$:Cr^{3+} SKLEIDIKLIO OPTIMIZAVIMAS